Temperature-dependent mechanism of magnetization-reversal processes in the spintronic electrode material $La_{0.67}Sr_{0.33}MnO_3$

W. Yan[1,2*], L. C. Phillips[1] and N. D. Mathur[1,**]

[1]Department of Materials Science, University of Cambridge, Cambridge, CB3 0FS, UK.
[2]School of Physics & Astronomy, University of Nottingham, Nottingham, NG7 2RD, UK
*email: wenjing.yan@nottingham.ac.uk
**email: ndm12@cam.ac.uk

We investigate magnetization-reversal processes in half-metallic epitaxial films of $La_{0.67}Sr_{0.33}MnO_3$ on $SrTiO_3$ (110) substrates. At 150 K, major-loop magnetization reversal (MLMR) occurs beyond minor-loop switching fields, implying that MLMR is limited by domain nucleation. At 280 K, MLMR overlaps with minor-loop switching fields if there are deliberately introduced precipitates, implying that the precipitates limit MLMR by pinning domain walls. To confirm that the precipitates pin domain walls at 280 K, we use a two-dimensional analogue of the Gaunt pinning model to show that pinning-limited switching occurs at fields consistent with the observed precipitate density of 0.3-2.0 μm^{-2}. Our work demonstrates that comparing major and minor loops at any temperature of interest represents a simple way to check whether spintronic electrode materials show nucleation-limited MLMR, as circumstantially required for single-domain switching in micron-scale elements of $La_{0.67}Sr_{0.33}MnO_3$ that represent spintronic electrodes [*Phys. Rev. Appl.* **4**, 064004 (2015)].

I. INTRODUCTION

Spintronic devices exploit the spin of the electron to store and process information. They currently include commercial magnetic sensors [1] and magnetoresistive random-access memory (MRAM) [2], and may in future include devices that integrate memory and logic [3-5]. Good spintronic performance depends on the performance of the magnetic electrodes, whose parallel and antiparallel magnetizations yield low and high states of two-terminal electrical resistance, respectively. The ferromagnetic perovskite $La_{0.67}Sr_{0.33}MnO_3$ (LSMO) is a particularly attractive spintronic electrode because it is fully spin polarized at low temperature, and has thus been used in magnetic tunnel junctions [6-12], molecular spintronic devices

[13-14], and long-distance spin transport through carbon nanotubes [15] and graphene [16]. However, the large low-temperature magnetoresistance (MR) in these devices tends to deteriorate at higher temperatures, falling to zero well below the Curie temperature of $T_C \sim 370$ K. This fall is traditionally associated with the suppression of T_C at interfaces and surfaces [17-19], but hitherto it has not been widely appreciated that this fall can also arise if magnetization reversal no longer proceeds by sharp switching at higher temperatures [20]. Here we show that for any given temperature below T_C, macroscopic magnetization data for unpatterned films (with and without precipitates) can—and should—be used to identify magnetization-reversal processes in order to predict whether patterned elements will display the single-domain switching required of spintronic electrodes.

It is well known in the context of permanent magnets [21] that magnetic switching is affected by both magnetic anisotropy and microstructure. In small and microstructurally homogeneous samples, magnetization reversal occurs via coherent rotation and curling processes that are primarily parameterised by magnetic anisotropy alone. In large samples, magnetization reversal requires nucleation of domains at surfaces and defects, as well as depinning of domain walls (DWs) that then propagate, such that the coercive field H_c is determined by the field required for nucleation or depinning, whichever is larger. In traditional hard magnets such as Nd-Fe-B [22] and Sm-Co [23-24], whose complex microstructures are designed to increase coercivity, the dominant magnetization-reversal mechanism is typically difficult to establish because it involves temperature-dependent transitions between nucleation-limited regimes and pinning-limited regimes [22-24]. Intriguingly, no such regimes have been identified in epitaxial thin films of the well known spintronic electrode material LSMO [6-16].

Magnetization reversal that involves nucleation and/or pinning has previously been identified in films of LSMO (110) and LSMO (001) by measuring the angular dependence of major-loop coercivity [25-26] (we index LSMO films as pseudocubic throughout this paper). However, nucleation-limited processes could not be distinguished from pinning-limited processes, and the measurements were performed at room temperature only. Here we use precipitate-containing epitaxial films of LSMO (110) to show that comparing major and minor easy-axis magnetic hysteresis loops [20,31] can distinguish nucleation-limited MLMR at 150 K from pinning-limited MLMR at 280 K. Our findings reveal that precipitates confer complexity on epitaxial films, just as microstructure confers complexity on permanent magnets [22-24]. We chose LSMO (110) over LSMO (001) because it is known from magnetic imaging that sufficiently small (5 μm × 5 μm) elements of precipitate-free LSMO films at 150 K show

nucleation-limited single-domain magnetization reversal if (110) oriented, and pinning-limited gradual magnetization reversal if (001) oriented [16,20]. Therefore LSMO (110) constitutes a suitable host in which to introduce temperature-dependent magnetization-reversal processes via precipitates, whose role we confirm using a 2D Gaunt pinning model that we derive from the 3D Gaunt pinning model [27].

The thermally driven transition from nucleation-limited MLMR to pinning-limited MLMR represents a hitherto neglected reason for poor spintronic performance. More generally, magnetization reversal processes identified at one temperature cannot be assumed to hold at other temperatures, such that magnetization-reversal processes should be tested at any given temperature of interest. Our work on continuous films of LSMO (110) shows that comparison of major and minor easy-axis magnetic hysteresis loops represents a simple way of checking whether magnetisation reversal is nucleation-limited, as required to anticipate single-domain magnetic switching in patterned elements such as spintronic electrodes.

II. METHODS

A. Experimental methods

Epitaxial films of LSMO (110) were grown on STO (110) by pulsed laser deposition as described in [17]. Two equivalent films [Film A (65 nm) and Film B (69 nm), Figs 1-3] were prepared along with a third sample [Film C (34 nm), Fig. 4] that was precipitate-free because we used an aperture to crop the inhomogeneous periphery of the laser beam [28]. Film C was thinner because we did not increase the number of laser pulses after cropping the beam, as increasing the number of pulses would have unduly compromised the LSMO target. However, the thinner film is equivalent to the thicker films both structurally and magnetically. Structural equivalence follows because even the thicker films are coherently strained (Fig. 1). Magnetic equivalence follows because even the thinner film is just thick enough to contain Bloch-like magnetic domain walls, as verified using micromagnetic simulations that are similar to those we show later.

Atomic force microscopy (AFM) was performed using a Digital Instruments Nanoscope (III). Film thickness, crystal structure and strain were studied using a PANalytical PW3050/65 X'Pert Pro high-resolution X-ray diffractometer. Magnetic measurements were made with a Princeton MicroMag 390 vibrating sample magnetometer (VSM). Prior to measuring minor

loops, LSMO films were demagnetized either by heating to 150 °C in air, or by applying an a.c. magnetic field whose magnitude was decreased by 1% per cycle.

B. Micromagnetic simulations

We use the OOMMF micromagnetic package [29] for simulations that are similar to those detailed in our previous work [20], except here we model infinite strips of width 1 μm with periodic boundary conditions that are implemented using the method described in [30]. The 1 μm strip width is much larger than our 34-65 nm film thickness, such that the aspect ratio of our unpatterned LSMO (110) films is represented sufficiently well. We use a cubic mesh whose 4 nm cell is similar to the LSMO exchange length $\sqrt{2A/\mu_0 M_s^2}$ = 3.9 nm (μ_0 is the permeability of free space). We use parameters (exchange constant A, saturation magnetisation M_s, in-plane uniaxial magnetic anisotropy constant K_{IP}) whose values are listed in Table 1 for each temperature of interest (150 K and 280 K), and we use out-of-plane anisotropy constant $K_{OOP} = 5.5\ K_{IP}$ (Appendix B).

III. RESULTS AND DISCUSSION

A. Structural data and magnetometry

First, we present structural and magnetic data for the two equivalent films that contain precipitates (Film A and Film B, Figs 1-3). Then we present structural and magnetic data for the film that contains no precipitates (Film C, Fig. 4).

AFM measurements of surface topography (Fig. 1a) reveal a film roughness of 0.1 nm and precipitates of width $W \sim 100$ nm, height ~ 4 nm, and areal density $\rho \sim 0.7$ μm^{-2}. Six similar measurements of different areas show that ρ varies in the range 0.3-2.0 μm^{-2}. An X-ray ω-2θ scan that includes the 220 reflection of the STO substrate (Fig. 1b) was used to evaluate an out-of-plane LSMO lattice parameter of 5.455 Å. This lattice parameter is consistent with the value in [25], and it is smaller than the value of 5.465 Å for bulk LSMO because the epitaxial film is under coherent in-plane biaxial tensile strain (Fig. 1c,d).

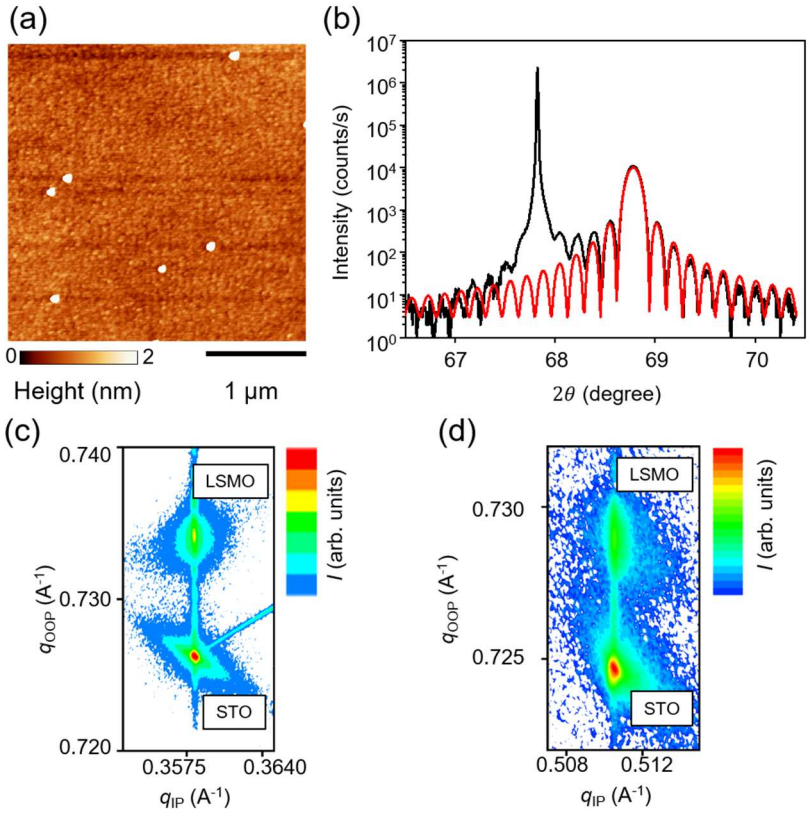

Figure 1. LSMO film characterization. (a) AFM image. (b) X-ray diffraction *ω-2θ* scan of LSMO//STO (black) showing the 220 reflection from the STO substrate (tallest peak) and the corresponding reflection from film (second-tallest peak, somewhat obscured by red fit data). Our fit (red) to the film data gives a film thickness of $t = 65$ nm. (c,d) X-ray reciprocal space maps around the (c) 130 and (d) 222 reflections of LSMO confirm that the film is fully strained. Reciprocal lattice units q_{IP} and q_{OOP} correspond to inverse lattice spacings along the in-plane (IP) and out-of-plane (OOP) directions, I denotes X-ray intensity. Data in (a,b) for Film A of thickness 65 nm, data in (c,d) for Film B of thickness 69 nm.

Epitaxial LSMO (110) films on STO (110) substrates possess an in-plane easy axis along the in-plane <100> direction, while the orthogonal in-plane and out-of-plane <110> directions are hard [28]. Fig. 2 presents a 280 K plot of the in-plane hard-axis magnetization M versus applied field H. The constant that describes the in-plane uniaxial magnetic anisotropy $K_{IP}(280\ \text{K}) = 4200\ \text{J m}^{-3}$ was determined from the data in Fig. 2 using the Stoner-Wohlfarth (SW) model [31]:

$$K_u \frac{M}{M_s} = \mu_0 M_s H \qquad \text{(Equation 1)}$$

where M/H was determined via a linear fit (red) to the data acquired during coherent rotation, and where saturation magnetization $M_s(280\ \text{K}) = 1.86\ \mu_B\ \text{Mn}^{-1}$. The corresponding values at 150 K are $M_s(150\ \text{K}) = 3.23\ \mu_B\ \text{Mn}^{-1}$ and $K_{IP}(150\ \text{K}) \sim 27800\ \text{J m}^{-3}$ (Appendix A).

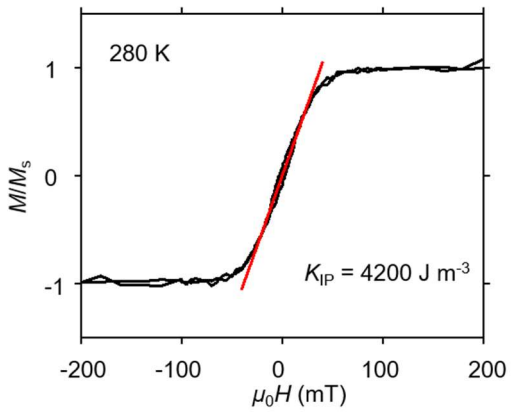

Figure 2. In-plane hard-axis LSMO magnetization at 280 K. Magnetization M versus collinear field H, with saturation magnetization $M_s = 1.86\ \mu_B\ \text{Mn}^{-1}$. The constant K_{IP} describing the in-plane uniaxial magnetic anisotropy was identified from the fit (red line) via Equation 1. Data for Film B, measured along the <110> direction that lies in-plane.

Magnetization reversal at 150 K and 280 K was studied at each temperature by comparing minor (black) and major (red) in-plane easy-axis hysteresis loops (Fig. 3a,b). The minor loops were measured by increasing the amplitude of the field in each consecutive cycle after having first demagnetized the sample to create domains, such that minor-loop switching is limited by DW depinning at pinning fields of $\pm H_p$. At 150 K, MLMR occurs beyond the range of pinning fields $\pm H_p$ identified from minor loops, and thus the major-loop switching fields are deduced to be nucleation fields $\pm H_n$ ($|H_n| > |H_p|$ implies nucleation-limited MLMR). At 280 K, MLMR occurs at fields that are similar to the range of pinning fields $\pm H_p$ identified from minor loops, and thus the major-loop switching fields are deduced to be pinning fields $\pm H_p$ that lie beyond unobserved nucleation fields $\pm H_n$ ($|H_n| < |H_p|$ implies pinning-limited MLMR). Increasing the temperature from 150 K to 280 K thus induces a transition from nucleation-limited MLMR to pinning-limited MLMR.

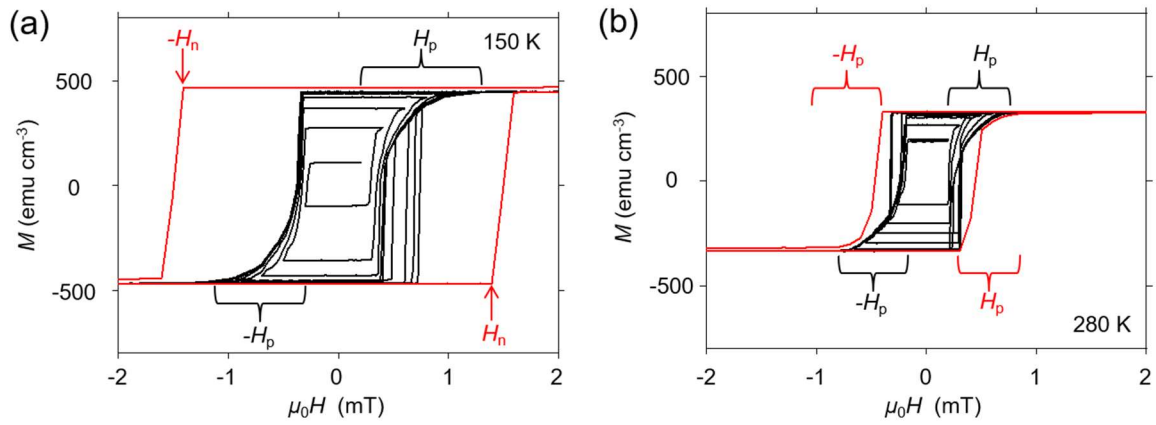

Figure 3. Transition from pinning-limited MLMR to nucleation-limited MLMR in LSMO (110). At (a) 150 K and (b) 280 K, we show in-plane easy-axis measurements of magnetization M versus field H. Major loops (red) are accompanied by minor loops (black) for which the film was demagnetized prior to increasing field amplitude in each consecutive cycle. In (a), $\mu_0|H_p| \sim 0.24$-1.28 mT (minor loops) is less than $\mu_0|H_n| \sim 1.4$ mT (major loop), so MLMR (red) is nucleation limited. In (b), $\mu_0|H_p| \sim 0.17$-0.71 mT (minor loops) has some overlap with $\mu_0|H_p| \sim 0.32$-0.8 mT (major loop), so MLMR (red) is pinning limited. Data for Film A, measured out to 100mT along the <100> direction that lies in-plane.

Let us now consider room-temperature magnetization reversal in our film with no precipitates (Fig. 4a) by comparing minor (black) and major (red) in-plane easy-axis hysteresis loops (Fig. 4b). MLMR (red data, Fig. 4b) occurs at fields that lie almost wholly beyond the range of pinning fields $\pm H_p$ identified from minor loops (black data, Fig. 4b), and thus the major-loop switching fields are deduced to be nucleation fields $\pm H_n$, such that MLMR in the precipitate-free film remains nucleation limited near room temperature. However, MLMR is not perfectly sharp because $|H_n|$ lies close to $|H_p|$.

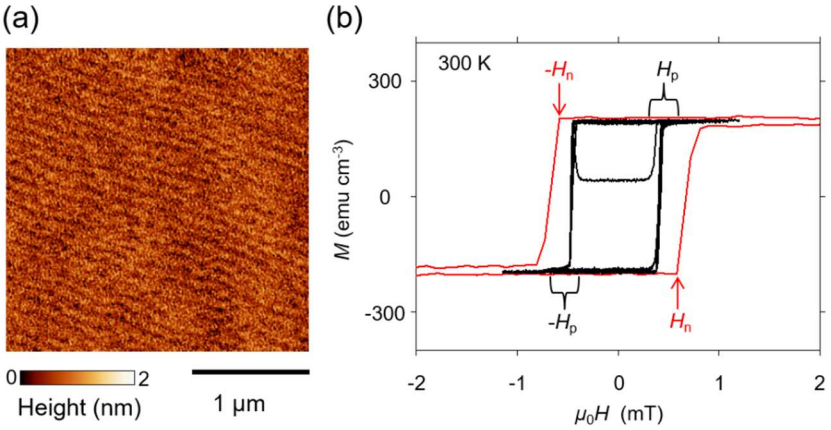

Figure 4. Nucleation-limited MLMR in precipitate-free LSMO near room temperature. (a) AFM image showing step-terrace growth with no precipitates. (b) In-plane easy-axis measurements of magnetization M versus field H at 300 K. The major loop (red) is accompanied by minor loops (black) for which the film was demagnetized prior to increasing the field amplitude in each consecutive cycle. Switching in the range $\mu_0|H_p| \sim 0.28$-0.72 mT (minor loop) is almost complete by $\mu_0|H| \sim 0.48$ mT, which lies below $\mu_0|H_n| \sim 0.58$ mT (major loop), such that MLMR (red) is nucleation limited. All data for Film C, magnetic measurements out to 300 mT along the <100> direction that lies in-plane.

B. Micromagnetic simulation

The micromagnetic OOMMF package was used to investigate DWs in 64 nm-thick LSMO films at both 150 K and 280 K (Fig. 5). The DWs at both temperatures are stable, Bloch-like, slightly asymmetric, and with little stray field, as expected for LSMO (110) [20], and more generally with similar input parameters [32]. The increase of total energy (stray field energy, demagnetizing field energy, exchange energy and anisotropy energy) due to the presence of a

DW is $\gamma = 103$ pJ m^{-1} (150 K) and 40 pJ m^{-1} (280 K) per unit length of DW. We find DW widths of $W_d = 2\sigma = 4$ nm (150 K) and 6 nm (280 K), where σ is the Gaussian standard deviation obtained from 1D plots of DW energy versus in-plane distance from the DW [these 1D plots of energy were obtained by averaging energy density maps (Fig. 5d,h) along the out-of-plane direction]. The simulated DW widths are much narrower than our precipitates of width $W \sim 100$ nm (Fig. 1b), implying that each precipitate wholly eliminates a DW segment of length W, thus saving energy γW. (It is possible that precipitates do not fully eliminate DWs [39], such that the energy saved is reduced by a small factor of $\alpha \sim 0.5$-1 to $\alpha\gamma W$, but we will assume $\alpha = 1$.)

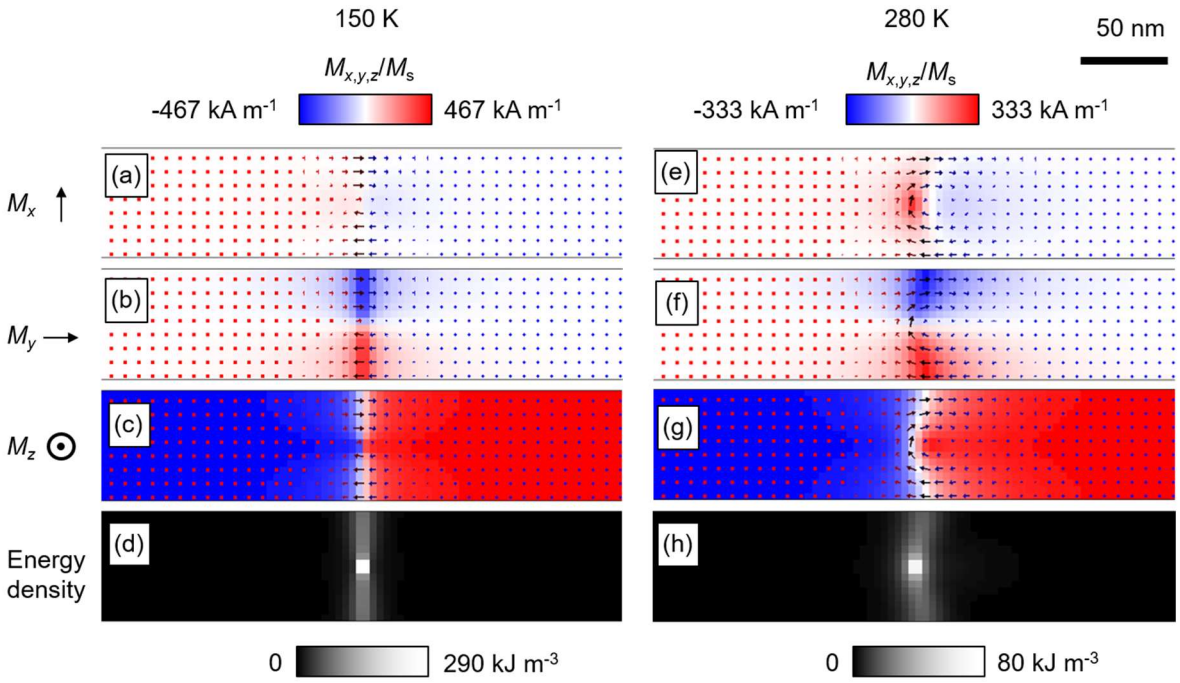

Figure 5. Simulations of magnetization and energy for a DW in 64 nm-thick LSMO (011) films. For (a-d) 150 K and (e-h) 280 K, all panels present the same *x*-*y* cross-section of the film containing a DW, and there is *z*-axis translational symmetry. Colour shading and arrows present the same information. Colour shading shows (a,e) M_x/M_s along the out-of-plane hard axis (a <110> direction), (b,f) M_y/M_s along the in-plane hard axis (a <110> direction), and (c,g) M_z/M_s along the in-plane easy axis (a <100> direction). Arrows show the local magnetization direction and are coloured red ($M_z/M_s > 0$), blue ($M_z/M_s < 0$) and brown ($M_z/M_s \sim 0$). M_s(150 K) = 467 kA m^{-1}, M_s(280 K) = 333 kA m^{-1}. (d,h) The corresponding energy density maps. Volume-normalized units are consistent with the *z*-axis translational symmetry.

C. 2D analogue of the Gaunt pinning model

The Gaunt pinning model [27] was used to derive a 2D Gaunt pinning model (Appendix C) from which we predict the DW pinning field H_{ep} (Table 1) due to an attractive pinning force f from precipitates:

$$H_{ep} = \frac{1}{\mu_0 M_s t}\left(\frac{f}{2}\right)^{\frac{3}{2}}\left(\frac{\rho}{\gamma}\right)^{\frac{1}{2}} \quad \text{(Equation 2)}$$

$$f = \frac{2\alpha\gamma W}{\left(W^2+W_d^2\right)^{\frac{1}{2}}}\exp\left(-\frac{1}{2}\right) \quad \text{(Equation 3)}$$

To remind, M_s is saturation magnetization, t is film thickness, ρ is areal precipitate density, γ is DW energy per unit length of DW, DW energy saving γW is reduced to $\alpha\gamma W$ if precipitates do not wholly eliminate DWs [39] (here we assume $\alpha = 1$), W is precipitate width, and W_d is DW width. In practice, our model predicts a range of pinning field H_{ep} values because the areal precipitate density ρ is presented as a range to reflect the observed variation.

T (K)	M_s (A m^{-1})	K_{IP} (J m^{-3})	K_d (J m^{-3})	A (J m^{-1})	γ (J m^{-1})	ρ (μm^{-2})	t (nm)	W (nm)	W_d (nm)	$\mu_0\lvert H_{ep}\rvert$ (mT)
150	4.67×10^5	2.78×10^4	1.72×10^6	2.1×10^{-12}	1.03×10^{-10}	0.3-2.0	65	100	4	0.88-2.27
280	3.33×10^5	4.2×10^3	8.75×10^5	1.2×10^{-12}	4.0×10^{-11}				6	0.48-1.23

Table 1. DW width and expected pinning field. For both 150 K and 280 K, domain wall width W_d and expected pinning field H_{ep} are derived from data in the other columns, via micromagnetic simulation and the 2D Gaunt pinning model, respectively. Variations of precipitate width W may be ignored as $W_d << W$ (Appendix C2).

At 150 K, our model predicts values of $\mu_0|H_{ep}| = 0.88\text{-}2.27$ mT, which are similar to the measured values of $\mu_0|H_p| = 0.24\text{-}1.28$ mT (minor loops, Fig. 3a). At 280 K, our model predicts values of $\mu_0|H_{ep}| = 0.44\text{-}1.13$ mT, which are similar to the measured values of $\mu_0|H_p| = 0.31\text{-}0.90$ mT (major loops, Fig. 3b) and $\mu_0|H_p| = 0.17\text{-}0.80$ mT (minor loops, Fig. 3b).

The transition from nucleation-limited MLMR to pinning-limited MLMR with increasing temperature can be understood via the following equations for nucleation and pinning fields (Appendix D):

$$H_p \propto M_s^{1.5}\ , \qquad \text{(Equation 4)}$$

$$H_n \propto bM_s^{2.3} - N_{d,eff}M_s, \qquad \text{(Equation 5)}$$

where b is a constant and $N_{d,eff}$ is the local demagnetizing factor at the most favourable nucleation site. On increasing the temperature, the fall in M_s would cause H_n to fall faster than H_p even without assistance from the $-N_dM_s$ term, such that H_p is liable to eventually exceeds H_n.

IV. CONCLUSIONS

For epitaxial films of LSMO (110) with precipitates in an otherwise microstructurally simple matrix, we have shown that increasing the temperature from 150 K to 280 K results in a transition from nucleation-limited MLMR to pinning-limited MLMR, consistent with a quantitative analysis in which we employed a 2D Gaunt pinning model that we derived from the 3D Gaunt pinning model [27]. For epitaxial films of LSMO (110) with no precipitates, we have shown that there is no such transition, thus confirming that the precipitates are responsible for the thermally driven change of MLMR mechanism. However, an absence of precipitates does not necessarily preclude pinning-limited magnetization reversal, as step edges and crystallographic defects can also pin DWs [34,35].

Given that the formation of magnetic domains during magnetization reversal severely compromises the performance of spintronic electrode materials [20], the pinning-limited MLMR that is responsible represents an important but hitherto neglected reason for the deterioration of spintronic device performance. Our simple method of studying magnetization reversal, which involves comparing major-loop and minor-loop switching fields [20,31], should be widely employed to confirm that major-loop switching fields lie beyond minor-loop switching fields at any temperature of interest. This would confirm that magnetization reversal is nucleation limited, and thus liable to proceed via single-domain switching in spintronic electrodes [20].

Appendix A: LSMO at 150 K

Changes of magnetic anisotropy due to changes of temperature (150 K ↔ 280 K) arise primarily due to changes of saturation magnetization M_s via [36-38]:

$$\frac{K_{IP}(280\ \mathrm{K})}{K_{IP}(150\ \mathrm{K})} = \left(\frac{M_s(280\ \mathrm{K})}{M_s(150\ \mathrm{K})}\right)^n. \qquad \text{(Equation A1)}$$

Using Film C, we establish $n = 3.3$ for the strained material (LSMO) by measuring $M_s(150\ \mathrm{K}) = 3.05\ \mu_B\ \mathrm{Mn}^{-1}$ at 150 K (Fig. 6a) and $M_s(280\ \mathrm{K}) = 1.70\ \mu_B\ \mathrm{Mn}^{-1}$ at 280 K (Fig. 6b), and by using the SW model (Equation 1) with these values and the fits shown to identify $K_{IP}(150\ \mathrm{K}) = 43000\ \mathrm{J\ m^{-3}}$ and $K_{IP}(280\ \mathrm{K}) = 6500\ \mathrm{J\ m^{-3}}$.

For Film B, we then identify $K_{IP}(150\ \mathrm{K}) \sim 27800\ \mathrm{J\ m^{-3}}$ from Equation A1 using $n = 3.3$, both $M_s(280\ \mathrm{K}) = 1.86\ \mu_B\ \mathrm{Mn}^{-1}$ and $K_{IP}(280\ \mathrm{K}) = 4200\ \mathrm{J\ m^{-3}}$ from the main text, and $M_s(150\ \mathrm{K}) = 3.23\ \mu_B\ \mathrm{Mn}^{-1}$ (Fig. 7).

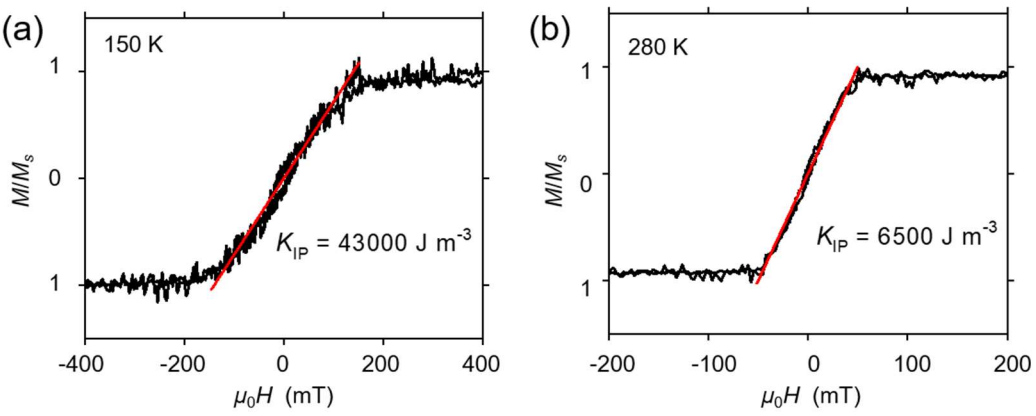

Figure 6. In-plane hard-axis LSMO magnetization at different temperatures. Magnetization M versus field H at (a) 150 K and (b) 280 K. In each panel, the red line fit was used to identify the anisotropy constant K_{IP} via Equation 1. Data for Film C, measured along the <110> direction that lies in-plane.

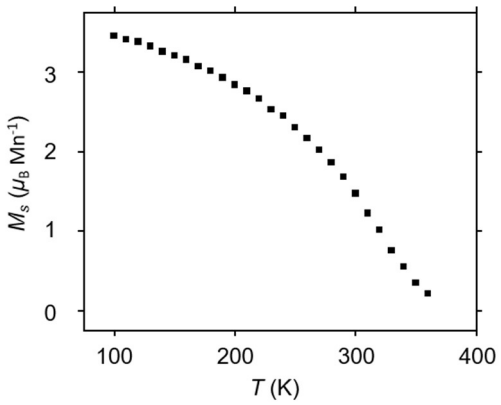

Figure 7. LSMO saturation magnetization versus temperature. Values of saturation magnetization M_s were obtained from in-plane easy-axis $M(H)$ measurements. Data for Film B, measured along the <100> direction that lies in-plane.

Appendix B: Out-of-plane anisotropy constant K_{OOP}

We use data for Film C at 300 K (Fig. 8) to determine the out-of-plane anisotropy constant K_{OOP} in terms of the in-plane uniaxial magnetic anisotropy constant K_{IP}, and we assume this ratio to hold for all temperatures of interest.

We find $K_{IP} = 6500$ J m^{-3} from Equation 1 given that a saturation magnetization of $M_s = 225$ emu cm^{-3} = 1.32 μ_B Mn^{-1} = 2.25×10^5 A m^{-1} is reached at a field of 0.47×10^5 A m^{-1} (corresponding to 0.06 T) (red data, Fig. 8).

We find $K_{OOP} = \frac{1}{2}\mu_0 M_s(H_{sat,OOP} - M_s) = 35700$ J m^{-3} given also that the field for saturation is 4.77×10^5 A m^{-1} (corresponding to 0.6 T) (black data, Fig. 8).

Therefore $K_{OOP}/K_{IP} = 5.5$, which we assume in our OOMMF simulations for both 150 K and 280 K.

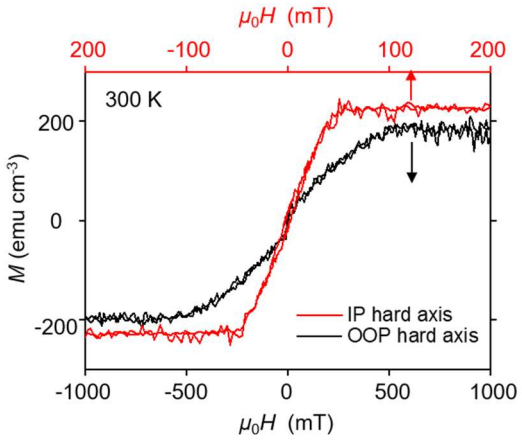

Figure 8: In-plane and out-of-plane magnetic anisotropy at room temperature. Red (black) data show the in-plane (out-of-plane) hard-axis magnetization M as a function of field H at 300 K. Data for Film C, measured along the <110> direction that lies in-plane (red) and the <110> direction that lies out-of-plane (black).

Appendix C: Derivation of the Gaunt pinning model

C1: Expression for the pinning field

The following represents a 2D version of the 3D derivation in [27].

Fig. 9 shows a 180° thin-film DW that is pinned between obstacles separated by distance $2L_1$. In magnetic field H, the DW bows out to perpendicular distance h_1 such that it forms an arc of radius R.

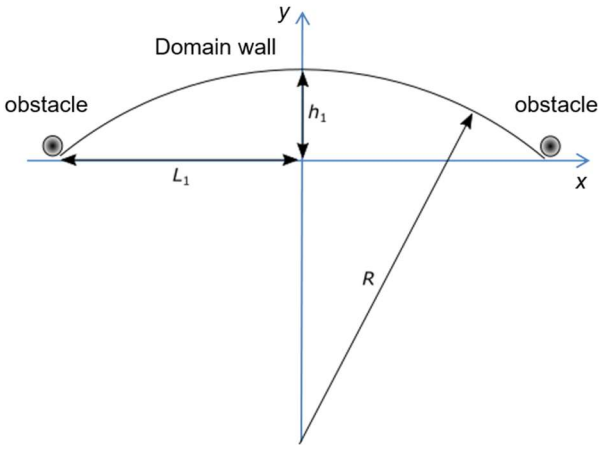

Figure 9. DW bowing in a magnetic field. The DW is pinned by two obstacles separated by $2L_1$. It forms an arc whose vertex lies at $(0, h_1)$.

If R is much greater than both L_1 and h_1 then we may approximately describe the arc as a parabola $y = f(x) = -ax^2 + h_1$, such that:

$$\begin{cases} f(L_1) = 0 \text{ and} & \text{(Equation A2)} \\ |\ddot{y}| = \frac{1}{R}, & \text{(Equation A3)} \end{cases}$$

where Equation A3 equates the second derivative of y to arc curvature $1/R$. From A2 and A3 we find:

$$y = -\frac{1}{2R}x^2 + h_1 \text{ and} \qquad \text{(Equation A4)}$$

$$h_1 \approx \frac{L_1^2}{2R}. \qquad \text{(Equation A5)}$$

The area enclosed between the DW and a straight line between the obstacles is found by integrating between $-L_1$ and $+L_1$, and using Equation A5 to yield:

$$A_1 = \int_{-L_1}^{L_1} \left(-\frac{1}{2R}x^2 + h_1 \right) dx \approx 2h_1 L_1 - \frac{L_1^3}{3R} = \frac{2L_1^3}{3R} \qquad \text{(Equation A6)}$$

Let us now consider two similar and adjacent DWs that are pinned by three collinear precipitates (each pair is separated by $2L_1$). If the DW breaks free from the central precipitate, then the situation in Fig. 8 is recovered with $L_2 = 2L_1$. The new area swept out by this event is:

$$\Delta A = A_2 - 2A_1 = \frac{4L_1^3}{R} \qquad \text{(Equation A7)}$$

In the strong pinning regime and under the Friedel steady-state criterion, we have $\rho \Delta A = 1$. This steady-state criterion states that the DW sweeps a volume containing, on average, one more precipitate during breakaway, where ρ is the areal density of pinning centres [27].

In a 2D thin film of thickness t, and during the breakaway event, the gain in DW energy equals exactly to the loss in magnetic energy, which is represented by the Laplace formula. The DW of line energy γ in J m^{-1} is:

$$\frac{\gamma}{Rt} = 2\mu_0 M_s H \qquad \text{(Equation A8)}$$

Using Equations A7 and A8, we can express the steady-state criterion as:

$$8L_1^3 \mu_0 M_s H \rho t = \gamma \qquad \text{(Equation A9)}$$

Therefore the value of the inter-obstacle distance $D = 2L_1$ for the steady state is:

$$D = \left(\gamma / \mu_0 M_s H \rho t \right)^{\frac{1}{3}} \qquad \text{(Equation A10)}$$

The expected coercive field when pinning is the limiting step $H_{ep} = f/2\mu_0 M_s D t$ (Equation 1 in [27]), which considers a single obstacle interacting with the DW, can then be derived if the maximum pinning force f of the pinning centre is known:

$$H_{ep} = \frac{1}{\mu_0 M_s t} \left(\frac{f}{2} \right)^{\frac{3}{2}} \left(\frac{\rho}{\gamma} \right)^{\frac{1}{2}} \qquad \text{(Equation A11)}$$

We will next derive the expression for the maximum pinning force f.

C2: Estimate of the maximum pinning force

Now that we have obtained the expression for H_{ep} in terms of the maximum pinning force, we will next derive the expression for the maximum pinning force f.

The maximum pinning force f is the maximum gradient in a plot of energy versus distance when a DW travels through and interacts with the precipitate. The form of this relation is generally non-trivial, assuming these precipitates are non-magnetic through-thickness particles as in [39], we may assume that the particle interrupts the DW, causing an attractive interaction due to reduced DW length. The peak interaction energy therefore equals to the energy associated with the missing DW, which is γW, where W is precipitate width. In the case where the precipitates are not through-thickness particles and cut through the domain wall partially, an additional factor α is required to describe the interaction energy $e_0 = \alpha\gamma W$.

We further assume that the energy-distance relation is a Gaussian in this form:

$$E(x) = e_0 e^{(\frac{-x^2}{2\sigma^2})}, \qquad \text{(Equation A12)}$$

where the standard deviation $\sigma = \frac{1}{2}\left(W^2+W_d^2\right)^{1/2}$ reflects the convolution of the particle width W with the domain width W_d. The maximum force $f = (\frac{dE}{dx})_{max}$ occurs at the inflection point $x = \pm\sigma$ of the Gaussian curve, such that:

$$f = \frac{e_0}{\sigma}\exp(-\frac{1}{2}) = \frac{2\alpha\gamma W}{(W^2+W_d^2)^{1/2}}\exp(-\frac{1}{2}) \qquad \text{(Equation A13)}$$

In the limit $W_d \ll W$, $f = 2\gamma \exp(-\frac{1}{2})$, i.e. f (and hence H_{ep}) are independent of W.

Combining Equation A11 and A13, we can quantitatively calculate the expected pinning field as a result of the presented precipitates as presented in Section C of the result and discussion.

Appendix D: Qualitative interpretation of the nucleation and pinning fields

Qualitatively, we can understand the transition from nucleation to pinning-limited reversal processes using scaling relationships developed in [27,33]. This is derived for a 3D material, as the scaling laws are better established. The pinning field H_p and nucleation field H_n are expressed as the following:

$$H_p \propto \rho_V f^2/\gamma_V M_s, \quad \text{(Equation A14)}$$

$$H_n \sim \frac{2K_{eff}}{\mu_0 M_S} - N_{d,eff} M_s, \quad \text{(Equation A15)}$$

where f is maximum restoring force of the pinning centre, ρ_V is the pinning centre density per unit volume V, γ_V is the DW energy per unit area, and where the effective anisotropy K_{eff} and demagnetizing factor $N_{d,eff}$ are difficult-to-estimate local parameters that describe the most favourable nucleation site.

Using $\gamma_V = \pi\sqrt{AK}$, where A is the exchange stiffness and $A \propto M^{5/3}$ [40], together with $f \propto \gamma_V$ [27] and $K_{eff} \propto M_s^a$ (a = 3.3, Appendix A), the above expression can be reduced to:

$$H_p \propto M_s^{\left(\frac{a}{2}-\frac{1}{6}\right)} = M_s^{1.5}, \quad \text{(Equation A16)}$$

$$H_n \propto (bM_s^{a-1} - N_{d.eff} M_s) = (bM_s^{2.3} - N_{d,eff} M_s), \quad \text{(Equation A17)}$$

where b is a constant and N_d is the demagnetizing factor.

Acknowledgements

We thank S. Chanattukuzhiyil and L. Fallarino for measuring some of the VSM data. This work was funded by a Schlumberger Cambridge International Scholarship and a University of University of Nottingham Anne McLaren Research Fellowship (W. Y.).

Data Availability

All data are presented in the manuscript, and available from the corresponding authors upon request.

References

1. B. Filipitsch and M. Ortner, Magnetic field distortion from conductive layers for high-frequency speed sensor applications, *IEEE Trans. Magn*. **53**, 4003604 (2017).
2. C. Chappert, A. Fert, and F. Nguyen Van Dau, The emergence of spin electronics in data storage, *Nat. Mater*., **6**, 813 (2007)
3. I. Žutić, J. Fabian, and S. Das Sarma, Spintronics: Fundamentals and applicatioins, *Rev. Mod. Phys*. **76**, 323 (2004)
4. H. Dery, P. Dalal, Ł. Cywiński and L. J. Sham, Spin-based logic in semiconductors for reconfigurable large-scale circuits, *Nature* **447**, 573 (2007)
5. B. Behin-Aein, D. Datta, S. Salahuddin and S. Datta, *Nature Nano* **5**, 266 (2010)
6. M. Bowen, M. Bibes, A. Barthélémy, J. –P. Contour, A. Anane, Y. Lemaître, and A. Fert, Nearly total spin polarization in $La_{2/3}Sr_{1/3}MnO_3$ from tunnelling experiments. *Appl. Phys. Lett*. **82**, 233 (2003).
7. J. Z. Sun, W. J. Gallagher, P. R. Duncombe, L. Krusin-Elbaum, R. A. Altman, A. Gupta, Y. Lu, G. Q. Gong, and G. Xiao, Observation of large low-field magnetoresistance in rilayer perpendicular transport devices made using doped manganate pervskites, *Appl. Phys. Lett.* **69**, 3266, (1996).
8. Y. Lu, X. W. Li, G. W. Gong, G. Xiao, A. Gupta, P. Lecoeur, J. Z. Sun, Y. Y. Wang, and C. P. Dravid, Large Magnetotunneling effect at low magnetic fields in micrometer-scale epitaxial $La_{0.67}Sr_{0.33}MnO_3$ tunnel junctions, *Phys. Rev, B* **54**, R8357 (1996).
9. C. Kwon, Q. X. Jia, Y. Fan, M. F. Hundley, D. W. Reagor, J. Y. Coulter, and D. E. Peterson, Large magnetoresistance in $La_{0.7}Sr_{0.3}MnO_3$/ $SrTiO_3$/ $La_{0.7}Sr_{0.3}MnO_3$ ramp-edge junctions, *Appl. Phys. Lett.* **72**, 486 (1998).
10. M. Bowen, A. Barthélémy, M. Bibes, E. Jacquet, J.-P. Contour, A. Fert, F. Ciccacci, L. Duo, and R. Bertacco, *Phys. Rev. Lett.* **95**, 137203 (2005).

11. V. Garcia, M. Bibes, L. Bocher, S. Valencia, F. Kronast, A. Crassous, X. Moya, S. Enouz-Vedrenne, A. Gloter, D. Imhoff, C. Deranlot, N. D. Mathur, S. Fusil, K. Bouzehouane, A. Barthélémy, ferroelectric control of spin polarisation, *Science*, **327**, 1106 (2010).
12. Y. W. Yin, J. D. Burton, Y-M. Kim, A. Y. Borisevich, S. J. Pennycook, S. M. Yang, T. W. Noh, A. Gruverman, X. G. Li. E. Y. Tsymbal, and Q. Li, Enhanced tunnelling electroresistance effect due to a ferroelectrically induced phase transition at a magnetic complex oxide interface, *Nat. Mater*. **12**, 397 (2013).
13. Z. H. Xiong, D. Wu, Z. Valy Vardeny, and Jing Shi, Giant magnetoresistance in organic spin-valves, *Nature*, **427**, 821 (2004).
14. D. Sun, M. Feng, X. Xu, L. Jiang, H. Guo, Y. Wang, W. Yang, L. Yin, P.C. Snijders, T. Z.Ward, Z. Gai, Z.-G. Zhang, H. Nyung Lee and J. Shen, Active control of magnetoresistance of organic spin valves using ferroelectricity, *Nature Commu.* **5**, 4396 (2014).
15. L. E. Hueso, J. M. Pruneda, V. Ferrari, G. Burnell, J. P. Valdés-Herrera, B. D. Simons, P. B. Littlewood, E. Artacho, A. Fert, and N. D. Mathur, Transformation of spin information into large electrical signals using carbon nanotubes, *Nature*, **445**, 410 (2007).
16. W. Yan, L. C. Phillips, M. Barbone, S. J. Hämäläinen, A. Lombardo, M. Ghidini, X. Moya, F. Maccherozzi, S. van Dijken, S. S. Dhesi, A. C. Ferrari, and N. D. Mathur, Long spin diffusion length in few-layer graphene flakes, *Phys. Rew. Lett*. **117**, 147201 (2016).
17. L. C. Phillips, F. Maccherozzi, X. Moya, M. Chidini, W. Yan, J. Soussi, S. S. Dhesi, N. D. Mathur, Tuning $La_{0.67}Sr_{0.33}MnO_3$ surface magnetism using $LaMnO_3$ and $SrTiO_3$ caps, *J. Magn. Magn. Mater,* **355**, 331 (2014).
18. J. –H. Park, E. Vescovo, H.-J. Kim, C. Kwon, R. Ramesh, and T. Venkatesan, Magnetic properties at surface boundary of a half-metallic ferromagnet $La_{0.7}Sr_{0.3}MnO_3$, *Phys. Rev. Lett.* **81**, 1953 (1998).
19. V. Garcia, M. Bibes, A. Barthélémy, M. Bowen, E. Jacquet, J. –P contour, and A. Fert, Temperature dependence of the interfacial spin polarisation of $La_{2/3}Sr_{1/3}MnO_3$, *Phys. Rev. B.* **69**, 052403 (2004).
20. L. Phillips, W. Yan, X. Moya, M. Ghidini, F. Maccherozzi, S. S. Dhesi, and N. D. Mathur, Control of magnetization-reversal mechanism via uniaxial anisotropy strength in $La_{0.67}Sr_{0.33}MnO_3$ electrodes for spintronic devices, *Phys. Rev. Appl*. **4**, 064004 (2015).
21. J. D. Livingston, A review of coercivity mechanism, *J. Appl. Phys.* **52**, 2544 (1981).
22. K.-D. Durst and H. Kronmüller, The coercive field of sintered and melt-spun NdFeB magnets, J. *Magn. Magn. Mater.* **68**, 63 (1987).

23. D. Goll, H. Kronmüller and H. H. Stadelmaier, Micromagnetism and the microstructure of high-temperature permanent magnets, *J. Appl. Phys*. **96**, 6534 (2004).
24. C. Rong, H. Zhang, B. Shen and J. Ping Liu, Mechanism of the anomalous temperature dependence of coercivity in Sm (Co, Fe, Cu, Zr)$_z$ high-temperature magnets, *Appl. Phys. Lett.* **88**, 042504 (2006).
25. H. Boschker, J. Kautz, E. P. Houwman, G. Koster, D. H. A. Blank and G. Rijnders, J. Appl. Phys. **108**, 103906 (2010).
26. M. Mathews, E. P. Houwman, H. Boschker, G. Rijnders and D. H. A. Blank, Magnetization reversal mechanism in $La_{0.67}Sr_{0.33}MnO_3$, *J. Appl. Phys.* **107**, 013904 (2010).
27. P. Gaunt, Ferromagnetic domain wall pinning by a random array of inhomogeneities, *Phil. Mag. B* **48**, 261 (1983).
28. W. Yan, Ph.D. thesis, Spin transport in few-layer graphene, University of Cambridge, UK, 2014. Available at https://doi.org/10.17863/CAM.84753.
29. M. J. Donahue and D. G. Porter, *OOMMF User's Guide*, Version 1.0 NISTIR 6376 (National Institute of Standards and Technology, Gaithersburg, MD, 1999).
30. K. M. Lebecki, M. J. Donahue and M. W. Gutowski, Periodic boundary conditions for demagnetization interactions in micromagnetic simulations, *J. Phys. D: Appl. Phys.* **41**, 175005 (2008).
31. B. D. Cullity and C. F. Graham, *Introduction to Magnetic Materials*, 2nd ed. (Wiley, Hoboken, NJ, USA, 2008).
32. K. Ramstöck, W. Hartung and A. Hubert, The phase diagram of domain walls in narrow magnetic strips, *Phys. Status Solidi (a)* **155**, 505 (1996).
33. J. M. D. Coey, *Magnetism and Magnetic Materials*, (Cambridge University Press, 2009).
34. P. Perna, C. Rodrigo, E. Jiménez, F. J. Teran, N. Mikuszeit, L. Méchin, J. Camarero and R. Miranda, Tailoring magnetic anisotropy in epitaxial half metallic $La_{0.7}Sr_{0.3}MnO_3$, *J. Appl. Phys*. **110**, 013919 (2011).
35. R. A. Hyman, A. Zangwill and M. D. Stiles, Magnetic reversal on vicinal surfaces, *Phys. Rev. B* **58**, 9276 (1998).
36. J. H. Van Vleck, On the anisotropy of cubic ferromagnetic crystals, *Phys. Rev*. **52**, 1178 (1937).
37. C. Zener, Classical theory of the temperature dependence of magnetic anisotropy energy, *Phys. Rev*. **96**, 1335 (1954).

38. J. Wang, H. Duan, X. Lin, C. Aguilar, A. Mosqueda, and G. Zhao, Temperature dependence of magnetic anisotropy constant in iron chalcogenide Fe3Se4: Excellent agreement with theories, *J. Appl. Phys*. **112**, 103905 (2012).
39. T. Higuchi, T. Yajima, L. Fitting Kourkoutis, Y. Hikita, N. Nakagawa, D. A. Muller and H. Y. Hwang, Mn_3O_4 precipitates in laser-ablated manganite films. *Appl. Phys. Lett.* **95**, 043112 (2009).
40. U. Atxitia, D. Hinzke, O. Chubykalo-Fesenko, U. Nowak, H. Kachkachi, O. N. Mryasov, R. F. Evans and R. W. Chantrell, Multiscale modelling of magnetic materials: Temperature dependence of the exchange stiffness, Phys. Rev. B 82, 134440 (2010).